ACSNANO

www.acsnano.org

ARTICLE

Chiral Optofluidics with a Plasmonic Metasurface Using the Photothermal Effect

Cuiping Ma, Peng Yu,* Wenhao Wang, Yisong Zhu, Feng Lin, Jiaying Wang, Zhimin Jing, Xiang-Tian Kong, Peihang Li, Alexander O. Govorov,* Dong Liu, Hongxing Xu,* and Zhiming Wang*

Cite This: https://doi.org/10.1021/acsnano.1c05658

ABSTRACT: Plasmonic metasurfaces with the photothermal effect have been increasingly investigated for optofluidics. Meanwhile, along with the expanding application of circularly polarized light, a growing number of investigations on chiral plasmonic metasurfaces have been conducted. However, few studies have explored the chirality and the thermal-induced convection of such systems simultaneously. This paper aims to theoretically investigate the dynamics of the thermally induced fluid convection of a chiral plasmonic metasurface. The proposed metasurface exhibits giant circular dichroism in absorption and thus leads to a strong photothermal effect. On the basis of the multiphysical analysis, including optics, thermodynamics, and hydrodynamics, we propose a concept of chiral spectroscopy termed optofluidic circular dichroism. Our results show that different fluid velocities of thermally induced convection appear around a chiral plasmonic metasurface under different circularly polarized excitation. The chiral fluid convection is induced by an asymmetric heat distribution generated by absorbed photons in the plasmonic heater. This concept can be potentially used to induce chiral fluid convection utilizing the chiral photothermal effect. Our proposed structure can potentially be used in various optofluidics applications related to biochemistry, clinical biology, and so on.

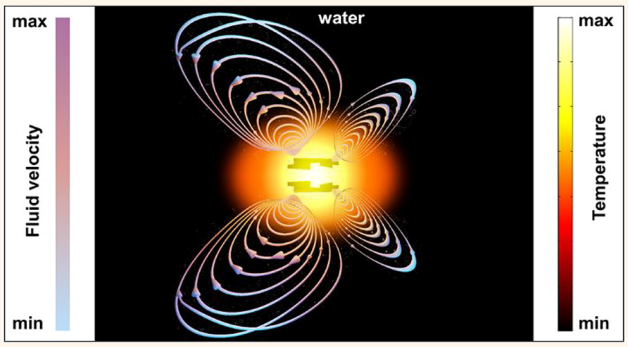

KEYWORDS: *optofluidics, chirality, fluid convection, circular dichroism, plasmonic absorber*

Optofluidics studies the control of the flow of fluids under optical excitation. A promising application of optofluidics is miniaturized lab-on-a-chip devices for analyzing and sorting particles and cells. Photoinduced heating in the liquid is attractive for dynamical optofluidic control because it is free of intricate fluid design, pumps, valves, or electrode patterning.[1−3] Metallic nanoparticles (NPs) support optically excited surface plasmons, in which conduction electrons oscillate coherently and feature light absorption enhancement. The associated heat generation and subsequent temperature rise in NPs have long been treated as side effects.[4] Because of the innovation of using plasmonic NPs as localized heat generators, thermoplasmonics turns this drawback into an asset and shows great potential in various applications, including plasmon-assisted magnetic recording,[5] opto-mechanics,[6] medical therapy,[7] thermal-catalysis,[8−10] bolometry,[11−13] and spatially resolved spectroscopies.[14,15] Therefore, controlling fluid by plasmonics is a natural means to engineer fluid motion at micro- or nanometer scale with degrees of dexterity.[4]

The past decade has witnessed a proliferation of studies in the field of thermoplasmonics-assisted optofluidics.[4] A resonant metallic NP can be heated to a temperature that can later modify its physical surrounding environment, such as the viscosity of the surrounding fluid.[16,17] Convection flow generated by the temperature gradient will break the original static state of the liquid around the heat source. This offers an idea for precise optical manipulation of motion of the cells and nanoparticles in an optofluidic channel.[16,18,19] Generally, the fluid convection can be controlled by the temperature increase, the size of the heat source, and the confinement of the fluid along the vertical direction.[4] For example, Quidant et al. investigated the dynamics of the thermal-induced fluid convection around a gold nanostructure,[17] where the motion of the fluid can be controlled by changing the height of the chamber. The fluid flow can also be controlled by the intensity and the polarization of light.[20] Strong and fast fluid convection

Received: July 4, 2021
Accepted: September 17, 2021

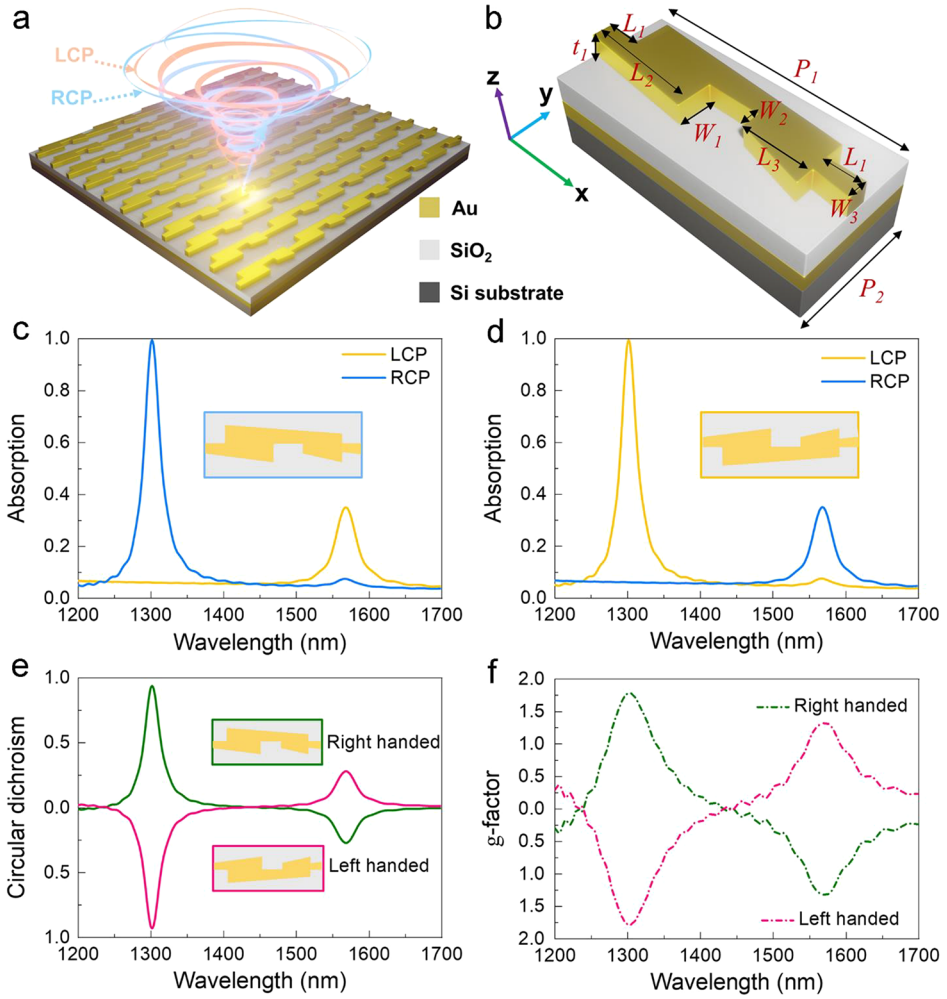

Figure 1. Optical response of chiral MPA. (a) Schematic of the chiral MPA consisting of Au nanoantenna arrays and a bottom Au film separated by a SiO_2 layer. (b) The geometry of a unit cell in the chiral MPA. The thicknesses of the top Au chiral structure and bottom Au layer are 55 and 100 nm, respectively; the thickness of the SiO_2 spacer is 150 nm. For the top resonator: L_1 = 100 nm, L_2 = 350 nm, L_3 = 200 nm, W_1 = 100 nm, W_2 = 50 nm, W_3 = 61 nm, P_1 = 800 nm, P_2 = 350 nm. Simulated optical response of RH (c) and LH (d) MPAs under RCP (blue) and LCP (yellow) illumination. (e) CD and (f) g-factor for RH (green) and LH (pink) MPAs. The surrounding media is air.

can be achieved by using plasmonic nanoantennas coupled to an indium−tin-oxide substrate[16] and bubble nucleation.[21,22] In addition, thermoplasmonics-induced convection flow can be applied for the assembly and deposition of NPs onto a substrate,[19] transportation of resonant NPs,[23] and optical sorting of exosomes.[24]

However, optical activity is an intrinsic property of many life-related substances, such as molecules, amino acids, DNA. It is now possible to artificially fabricate chiral plasmonic structures with more robust chiroptical and chiral photothermal responses than natural molecular systems because of the enhanced light−matter interaction.[13,25−28] Bridging optofluidics and chiral plasmonics create opportunities to sensing and manipulating of molecules in research fields where both chiroptical signals and aqueous environment are important, such as in biophysics, biochemistry, and life science. It would be possible to achieve polarization-selective trapping, sorting, and aggregating of chiral molecules such as proteins and DNAs and realizing them in a nanoscale cargo. In this paper, we theoretically study a type of chiral-optical-fluidic effect based on the photothermal circular dichroism (CD) of chiral plasmonic metasurfaces.[13] The optofluidic circular dichroism (OFCD) described in this paper stems from the strong asymmetry in the fluid convection induced by the chiral photothermal effect. Chiral metamaterial perfect absorbers (MPAs) are used to generate prominent optical and photothermal CD spectra. We observe that distinct velocity patterns of the fluid around the chiral nanoantennas are generated, that is, the photothermal CD (CD_T) could translate to fluid convection CD (CD_v). The strong optofluidic chiral effect suggests that the chiral MPAs are promising for manipulation of microfluid with circularly polarized light (CPL) and can be in general used for polarization-sensitive optofluidic applications and bioanalysis.

RESULTS AND DISCUSSION

Optical Properties of Chiral MPA. The chiral MPA (Figure 1a,b) consists of a periodic array of Au resonator and an Au backplane, separated by a SiO_2 layer. MPAs are typically composed of plasmonic resonators and a reflector separated by a dielectric layer.[12] The MPA not only improves the photothermal effect but also reduces the required light fluence to achieve a certain temperature increase.[29] Full-wave electromagnetic simulations are carried out to investigate the optical response of the chiral MPA. Left- and right-handed circularly

https://doi.org/10.1021/acsnano.1c05658
ACS Nano XXXX, XXX, XXX−XXX

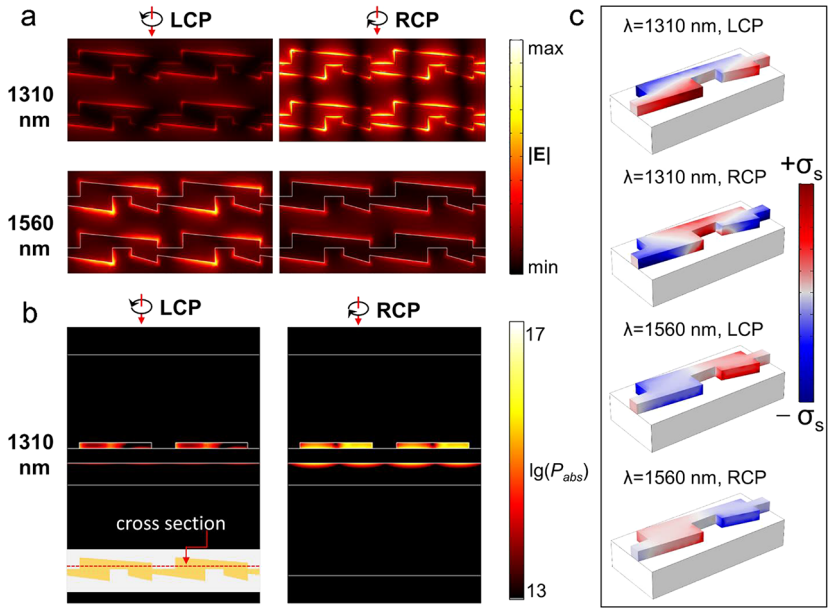

Figure 2. Near field properties of chiral MPA. (a) Spatial electric intensity profiles were taken on the top surface of the chiral structure at 1310 nm (the first row) and 1560 nm (the second row). (b) Absorption distribution under LCP (left) and RCP (right) illumination in the chiral MPA. The inset shows the position of the cross-section is along the red-dashed line. (c) Surface charge distributions for the two resonant modes, i.e., quadrupole modes and dipole. The top two and bottom two were recorded at 1310 and 1560 nm, respectively. The surrounding medium is air.

polarized (LCP and RCP) light is incident on the front side of the MPA. Figure 1c shows the simulated optical spectra of a right-handed (RH) MPA, which behaves as a perfect light absorber for RCP (i.e., absorptance $A_{RCP} \approx 1$) but a nonresonator for LCP incidence at the first resonant peak near λ = 1310 nm. Reversed results are observed for the left-handed (LH) enantiomer, as shown in Figure 1d for the absorption spectra with LCP and RCP incidences. The two spectral peaks at ∼1310 nm and ∼1560 nm originate from two distinct plasmonic resonance modes. The large difference in optical absorption for LCP and RCP light leads to a giant CD (CD_A) and g-factor (g_A-factor, g-factor without subscript refers to g_A -factor in this paper), which are defined as

$$CD_A = A_{LCP} - A_{RCP} \quad (1)$$

$$g_A = \frac{A_{LCP} - A_{RCP}}{(A_{LCP} + A_{RCP})/2} \quad (2)$$

Here A_{LCP} and A_{RCP} are the optical absorptance of the MPA under the incidence of LCP and RCP light, respectively. As shown in Figure 1e,f, the maximum CD is 0.94, and the g-factor of 1.78 can be achieved. The LH and RH enantiomers present an inverted spectrum of CD and g-factor. Taking the RH enantiomer as an example, we also investigated the phase change near the resonance wavelength to better understand the influencing factors of the giant CD. The maximum CD stems from the perfect absorption of RCP and complete reflection of LCP for the RH structure. Figure S1 plots the different phase change under LCP and RCP incidence. The phase of the *x*- and *y*-component reflection waves was demonstrated to compare with the absorption spectrum. It can be clearly seen that the absorption is almost zero under LCP incidence, and the phase is linear without sudden change. On the contrary, the MPA exhibits perfect absorption of RCP around 1310 nm, and the phase also undergoes a significant change at this position. Therefore, the phase mutation will directly affect the absorption of CPL and thus influence the CD.

Furthermore, the effects of the period P_2, the thickness of the dielectric layer, and the thickness of the chiral resonators on CD have been investigated, as shown in Figure S2. Because of the advantage of giant CD in absorption and inherent electrical connection, the MPA can be an ideal candidate for potential applications for circularly polarized light (CPL), such as hot electron photodetection, heat conversion, and thermal-induced fluid convection.[16,17,30,31] The g-factor of natural ingredients is usually around 10^{-7}−10^{-5} because of the small spatial extension of molecular wave functions compared to the wavelength of the incident light.[26,32] In contrast, the g-factor of artificial plasmonic nanostructures is much higher because of the plasmon-enhanced light−matter interactions. For example, the g-factor value is $\sim 10^{-3}$ for a DNA-bridged gold nanorod assembly.[33] A g-factor of 0.14 was demonstrated by the three-dimensional chiral plasmonic oligomers.[34] In planar chiral metamaterials or metasurfaces, the g-factor is even higher in both theory and experiment. In the previous work, we have proposed a zigzag-wire-shaped perfect absorber with a g-factor value up to 1.52.[9] In the present work, the particular permutation of four right-angled trapezoids with different sizes achieves a very strong mirror asymmetry, leading to a huge absorption difference for LCP and RCP light. Thus, an ultrahigh g-factor value can be obtained in this work. According to eq 2, the value of the asymmetry g-factor reaches 1.78, which surpasses the values mentioned in ref 9 and is very close to the theoretical upper limit of 2. Therefore, the giant absorption CD in the chiral MPA can be used for CD_T.[9,13] It is worth mentioning that our proposed MPA's chirality is significantly higher than any other chiral structures operating at visible and NIR regions. In Table S1, we present a comparison of the calculated g-factor and CD values with other examples.

https://doi.org/10.1021/acsnano.1c05658
ACS Nano XXXX, XXX, XXX−XXX

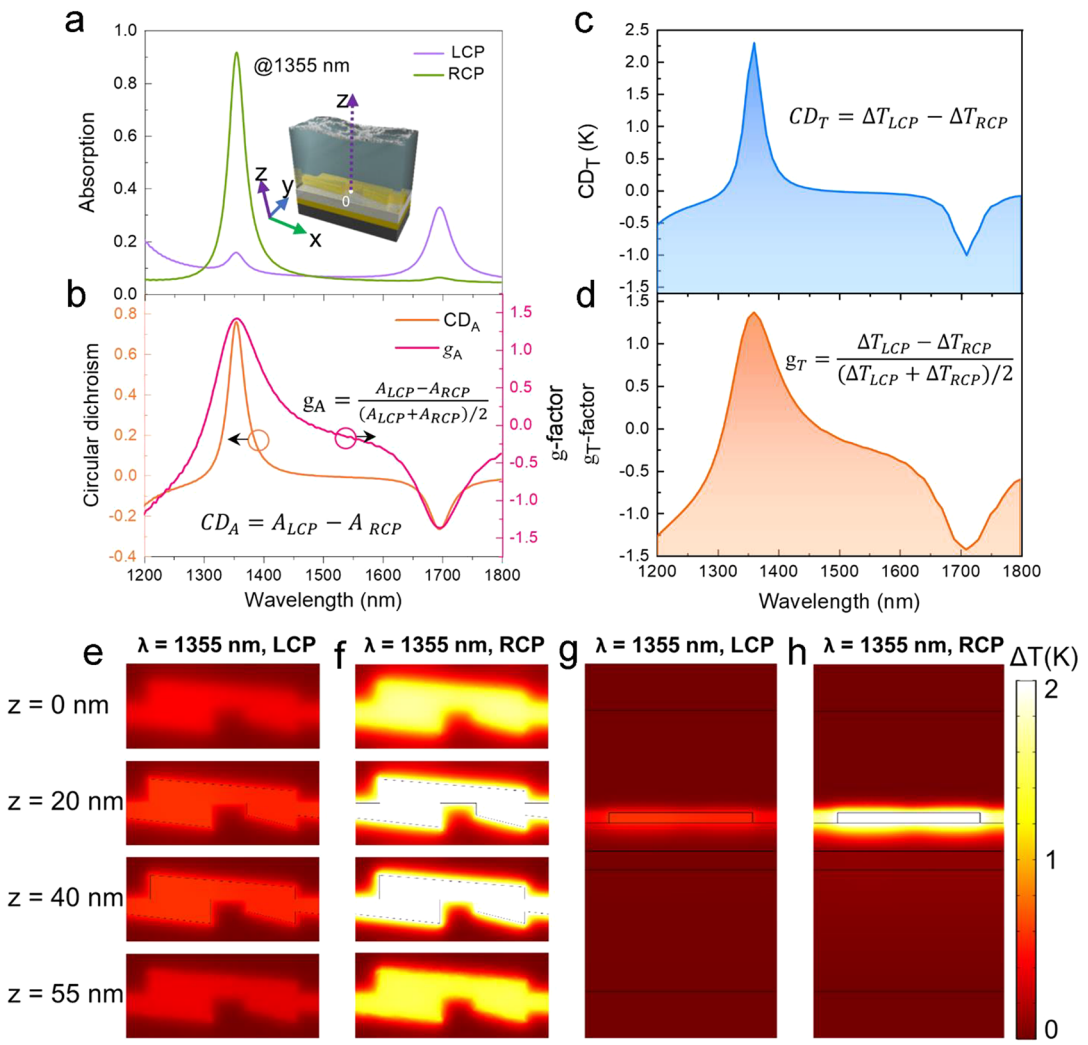

Figure 3. Photothermal effect of MPA in water. (a) Simulated optical response of RH MPA under RCP (green) and LCP (purple) illuminations. The inset shows the schematic of MPA in water. (b) Optical CD (orange) and g-factor (pink) for RH MPA. (c) Photothermal CD spectra, $CD_T(\lambda)$. (d) Spectra of the thermal g-factor, g_T (λ). (e–h) Photoinduced temperature increase, ΔT, at the wavelength λ = 1355 nm. (e, f) in the horizontal cross sections (z = −20, 0, 40, and 70 nm) and (g, h) in the vertical section (y = 20 nm). (e, g) LCP incidence; (f, h) RCP incidence. The incident light flux is $I_0 = 10^4$ W/cm^2. The data are given at the time of t = 8 ns.

The top Au resonator induces chiral optical effects that stem from the cross-coupling between the electric and magnetic response, that is, excitation of **E**-field excited magnetic dipoles and **H**-field excited electric dipoles. The electromagnetic field distributions at resonant wavelengths are shown to demonstrate the underlying physical processes. The simulated **E**-field distributions and enhancement are entirely different between the LCP and RCP incident light, as shown in Figure 2a. In a typical MIM absorber, electric and magnetic resonance will induce antiparallel current flow on the top and bottom layers. The magnetic field enhancement is shown in Figure S3a. Herein, the absorption loss is mainly located in the top resonator, as shown in Figure 2b, originating from the enhanced fields localized at the resonators. Figure 2c demonstrates the surface charge distributions of the chiral MPA at two resonant wavelengths under LCP and RCP illumination. At the wavelength of 1310 nm, the perfect absorption originates from higher-order quadrupole resonance, while at 1560 nm, the absorption originates from dipole resonance. Again, the surface charge distributions show different profiles under CPL, corresponding to the **E**-field profile, as shown in Figure 2a. The response of the chiral MPA to linearly polarized light is also studied to understand the origin of the strong CD, as shown in Figure S3b. The electric field vector of CPL can be decomposed into two orthogonal linearly polarized light electric field vectors, E_x and E_y, that oscillate with a 90-degree phase shift between them. The complex amplitudes for LCP and RCP light are given by

$$\mathbf{E}_{\mathrm{LCP}} = \frac{1}{\sqrt{2}}\left(1,\ \exp\left(-\frac{\pi}{2}\mathrm{i}\right)\right)^{\mathrm{T}} \tag{3}$$

$$\mathbf{E}_{\mathrm{RCP}} = \frac{1}{\sqrt{2}}\left(1,\ \exp\left(\frac{\pi}{2}\mathrm{i}\right)\right)^{\mathrm{T}} \tag{4}$$

Two linearly polarized light with the electric field vector along the x-axis (L_x) and y-axis (L_y) is used to illuminate the chiral MPAs, as depicted in Figure S3c. Taking the RH structure as an example, the RH enantiomer shows a strong response under RCP light, resulting from constructive interaction between the L_x and L_y modes. At the resonant wavelength, 1310 nm, where the RCP response is close to the

https://doi.org/10.1021/acsnano.1c05658
ACS Nano XXXX, XXX, XXX−XXX

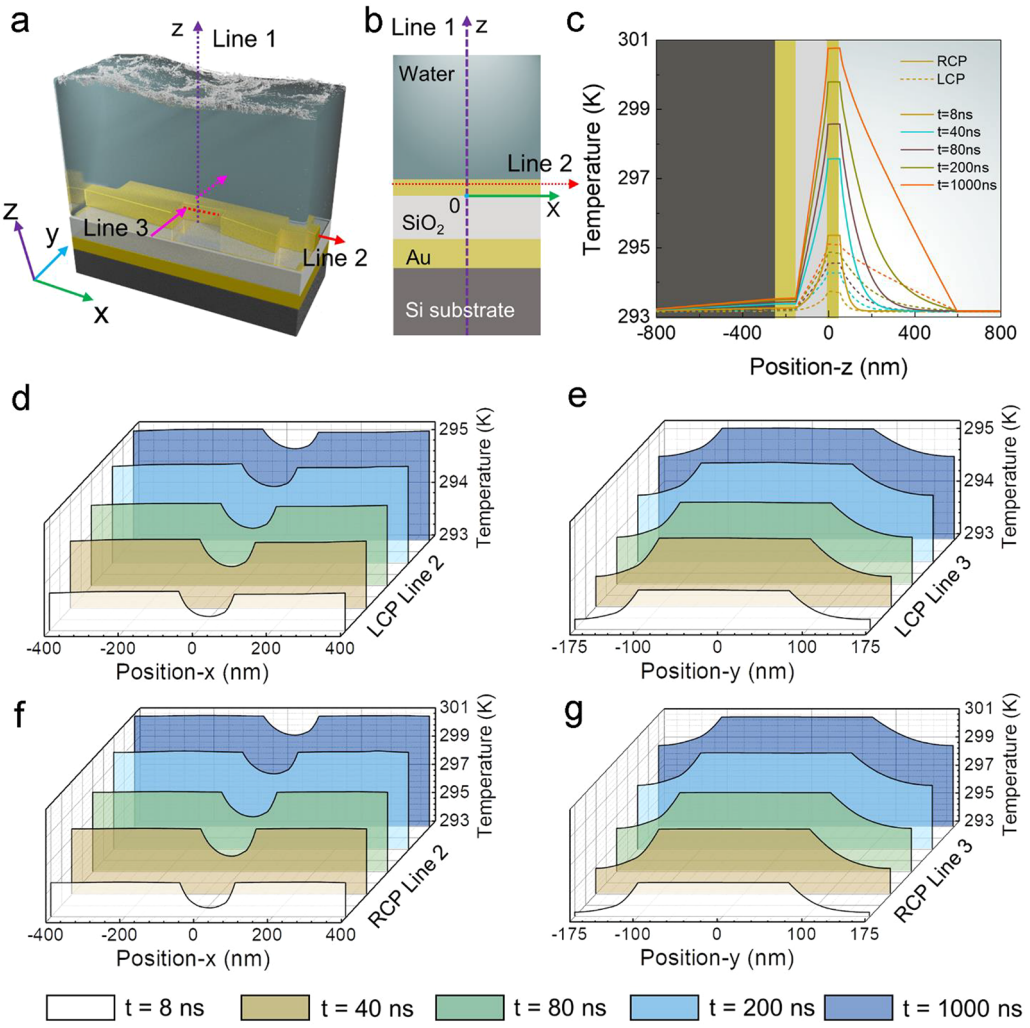

Figure 4. Spatial-temporal temperature distribution of MPA in water. (a) Geometry and (b) vertical schematic of the MPA in water. (c–g) Spatial-temporal distribution in the MPA at t = 8 ns, 40 ns, 80 ns, 200 ns, 1000 ns with (c) along the vertical z-axis (*Line 1*), (d, f) along *Line 2*, and (e, g) along *Line 3*. Panels (d, e) and (f, g) show the spectra with the incidence of LCP and RCP beams.

sum of the absorption from L_x and L_y polarization, the CD signal is maximized, as shown in Figure S3b. In contrast, the absorption of the chiral MPA under LCP light is approximate to the difference between L_x and L_y modes because the two modes have a negative interference from the out-of-phase linear mode under LCP illumination.[9] The discussion applies to LH enantiomer and *vice versa*.

Photothermal Circular Dichroism of the Chiral MPA. We next study the photothermal response of the MPA in the aqueous environment. The resonant peak is shifted from ~1310 nm to ~1355 nm because of the surrounding refractive index change from the air to water, as shown in Figure 3a, resulting in CD approaching 0.8 and g_A-factor of 1.42, as shown in Figure 3b. We use our previously proposed formulas, that is, CD_T and g-factor for the photothermal CD (g_T-factor), to evaluate the asymmetry of photoinduced temperature:[13]

$$CD_T(\mathbf{r}) = \Delta T_{LCP}(\mathbf{r}) - \Delta T_{RCP}(\mathbf{r}) \quad (5)$$

$$g_T = \frac{\Delta T_{LCP}(\mathbf{r}) - \Delta T_{RCP}(\mathbf{r})}{[\Delta T_{LCP}(\mathbf{r}) + \Delta T_{RCP}(\mathbf{r})]/2} \quad (6)$$

where $\Delta T_{LCP}(\mathbf{r})$ and $\Delta T_{RCP}(\mathbf{r})$ are the local temperature increase induced by LCP and RCP light, respectively. The strong CD further leads to a strong photothermal CD effect in the water, as shown in Figure 3c. Similarly, the thermal g_T-factor presents the resemble trend of the CD_T spectra, as shown in Figure 3d. CD_T is consistent with the absorption CD spectrum, and the amplitudes of the g_A-factor and the g_T-factor have similar magnitudes, indicating that the enhanced photothermal CD originates from plasmonic resonances from the chiral MPA. The maximum CD_T value is 2.30 K at the irradiation time t = 8 ns, and g_T-factor value is about 1.38. The incident flux of light is expressed by $I_0 = c_0|\mathbf{E}_0|^2\varepsilon^{1/2}/8\pi$, where $\mathbf{E}_0$ is the amplitude of the incident field, and c_0 is the speed of light in a vacuum. It should be noted that a small incident flux, $I_0 = 10^4$ W/cm^2, is employed in our research on the photothermal effect in this paper. If the incident flux, $I_0 = 10^5$ W/cm^2 as used in ref 13, is introduced in our calculation, the maximum CD_T value will be 23.00 K, which is higher than most previous reports. Thus, the chiral photothermal effect is also mainly dependent on the illumination intensities. However, the small light intensity is favored in microfluidic devices for chip-based chemical and biological analyses. For example, a highly focused nanosecond pulsed laser was used to form plasma and cavitation bubbles in the mixed fluids, but the shortcoming of this method is that extremely high intensity of

https://doi.org/10.1021/acsnano.1c05658
ACS Nano XXXX, XXX, XXX–XXX

7.6×10^{10} W/cm^2 is required, leading to side effects, for example, photodamage in the biological application.[35]

Figure 3e–h and Figure S4 demonstrate a local temperature increase in the RH MPA in water and air at different positions under the LCP and RCP light, respectively. The local temperature increase is determined by

$$\Delta T(r, t) = \frac{Q(r, t)}{4\pi\kappa_s R_L} \tag{7}$$

where $Q(r, t)$ is the local heat power intensity; κ_s and R_L are the thermal conductivity of the surrounding medium and the Laplace radius of the particle;[1] r, t are the coordinate and time, respectively. The $Q(r, t)$ comes from the light dissipation in the system:

$$Q(r, t) = \frac{\omega}{2} Im(\varepsilon(\omega))\varepsilon_0 |\mathbf{E}(r, t)|^2 \tag{8}$$

The thermal power inside the chiral nanostructure is proportional to the square of the excitation electric field. There is no heat generated outside the resonator since the light absorption of water is negligible. Therefore, the heat transferring from the metallic resonator source to the surrounding water is governed by the heat transfer equation:[17]

$$\rho c_p\left[\frac{\partial}{\partial t}T(\boldsymbol{r}, t) + \nabla\cdot(T(\boldsymbol{r}, t)\mathbf{v}(\boldsymbol{r}, t))\right] - \kappa\nabla^2 T(\boldsymbol{r}, t) = 0 \tag{9}$$

where ρ and c_p are density and specific heat capacity at a constant pressure of water, respectively. κ is the thermal conductivity of water, $\mathbf{v}(\boldsymbol{r}, t)$ is the velocity of the fluid, $\nabla^2 T(\boldsymbol{r}, t)$ is an additional nonlinear convective term. The positions z = 0 nm and z = 55 nm correspond to the bottom and top surfaces of the chiral structure, respectively. The positions z = −20 nm and z = 70 nm are taken at 20 and 15 nm from the bottom and top of the chiral resonator, respectively. It is clearly shown that the local temperature increments are concentrated around the top chiral resonators because of the nonradiative decay of plasmonic resonances. Because of the high thermal conductivity of gold, the spatial maps of the photoinduced temperature in top metallic resonators are nearly identical and distribute uniformly, as shown in Figure 3g, h, and Figure S4e–h. The local temperature rise rapidly decreases when moving away from the top resonators both in the lateral and vertical directions.

To further investigate the photothermal effect of our metasurface, we plot the spatial-temporal temperature distribution along with different-marked lines, as shown in Figure 4a,b. The spatial-temporal temperature distribution is investigated to further understand the effects of the temperature change on the velocity of the liquid in the following discussion. We observed the spatial-temporal distribution as a function of time with *Line 1*, as shown in Figure 4c. The temperature distribution in the metal is nearly flat because of the high thermal conductivity of gold. The heat diffuses into the surrounding material, leading to decayed temperature. As time increases, the enhanced diffusive spreading of the local heat is observed. Spatial-temporal distributions of *Line 2* and *Line 3* under various irradiation times are plotted in Figure 4d–g. It can be seen that the longer laser irradiation time leads to a higher temperature increase, and the temperature under RCP irradiation is higher than that under LCP irradiation because of the selective absorption of the chiral MPA.

To better understand the saturation state of the system, we further studied the photothermal conversion efficiency (PTE) of the proposed MPA. We define the photothermal conversion efficiency (PTE) as the ratio of the internal energy increase of the system to the total energy incident on the system. The internal energy increase of the system can be divided into two parts, one is the energy increase of water and the other is the heat absorbed by the resonator. The equation can be expressed as[36]

$$\eta = \frac{c_w m_w \Delta T_w + c_n m_n \Delta T_n}{I A \Delta t} \tag{10}$$

where I and A refer to the incident light flux intensity and the surface area exposed to CPL radiation absorbance. c, m and ΔT are the specific heat capacity, mass, and the average temperature increase, respectively, with the subscripts "w" and "n" refer to water and chiral resonators. Δt is the irradiation time. The thermal energy converted from the laser energy absorbed by MPA can be expressed as

$$Q_i = IA\eta \tag{11}$$

The temperature of the system can be expressed as[37]

$$(c_w m_w + c_n m_n)\frac{dT}{dt} = Q_i - Q_C - Q_r \tag{12}$$

Q_c is the energy transferred to the external environment through heat conduction, which can be expressed as

$$Q_c = B(T - T_{amb}) \tag{13}$$

where B is thermal conductivity coefficient from solution to the external environment and T_{amb} is environment temperature. Q_r is the energy loss through thermal radiation, which can be neglected due to the low-temperature structure.[36] By solving eqs 11–13, the time-varying temperature of the solution can be expressed as[37]

$$T = T_{amb} + \frac{IA\eta}{B} + be^{-Bt/c} \tag{14}$$

where b is a specific coefficient that can be obtained through experiment. There will be $e^{-Bt/c} \approx 0$ if the irradiation time is long enough. Then the temperature will reach a saturation state:

$$T = T_{amb} + \frac{IA\eta}{B} \tag{15}$$

Figure S5 shows the spectra of the photothermal CD with different incident flux and irradiation times. It can be seen that when the incident flux is set to 1×10^4 W/cm^2, CD_T gradually increases and reaches a stable value with the extension of the irradiation time. In a short irradiation time, a small time change can cause a relatively significant temperature rise. The rate of temperature rise decreases with the extension of irradiation time. The time of saturation of the MPA is the order of 1000 ns. The increase of the laser intensity will lead to a corresponding increase of CD_T. There is a linear relationship between photothermal CD and irradiation energy. The calculated PTE of the RH structure is shown in Figure S6. It presents anisotropic PTE under LCP and RCP, and for the RH enantiomer, the maximum PTE can achieve ∼42% under RCP light.

Optofluidic Circular Dichroism. Uneven heat distribution was generated around the resonator controlled by chiral

https://doi.org/10.1021/acsnano.1c05658
ACS Nano XXXX, XXX, XXX–XXX

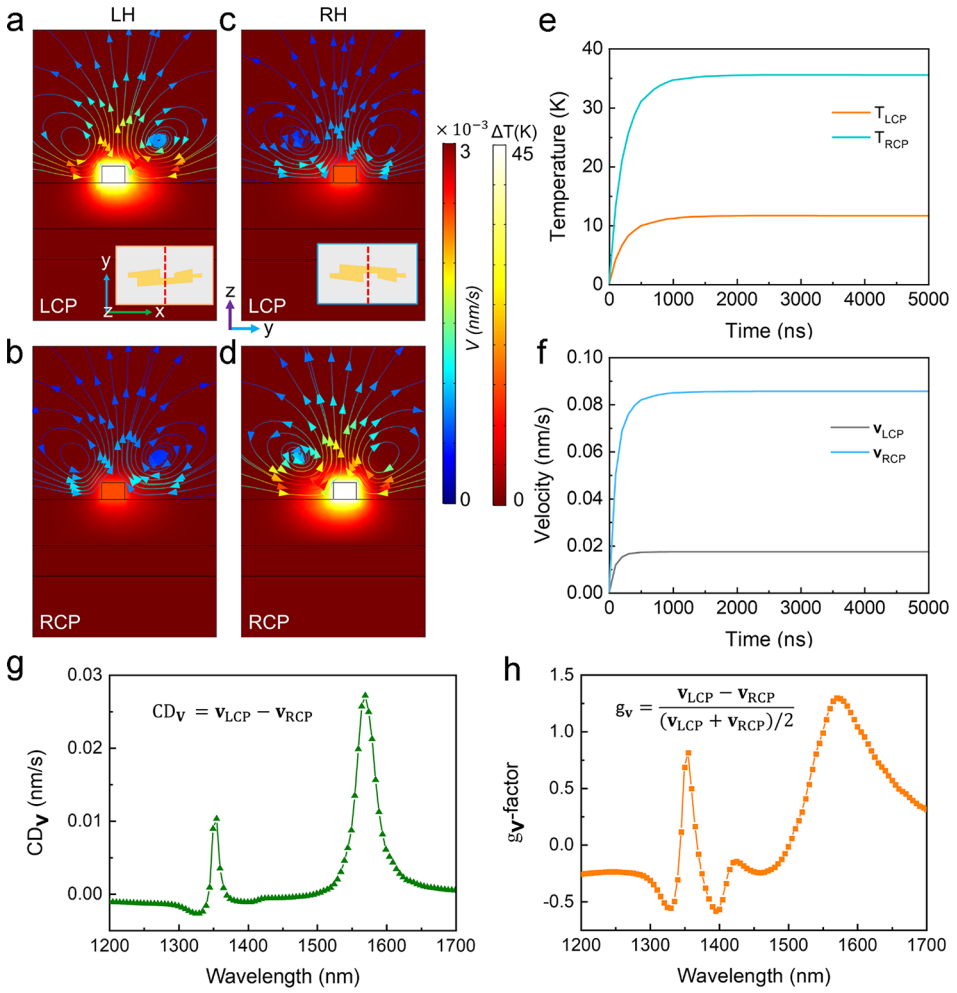

Figure 5. Thermal-induced chiral fluid convection of MPA. (a–d) Temperature and velocity patterns (streamlines) at t = 8 ns. The insets show the schematic of the top view of a chiral unit cell with LH structure (a) and RH structure (b); red dashed lines indicate the position of the vertical section of (a–d). Panels (a, b) are taken from the LH structure and panels (c, d) are taken from the RH structure under the illumination of LCP (a, c) and RCP (b, d), respectively. (e) Average temperature increase of the liquid as a function of time under LCP (orange) and RCP (turquoise) at the resonant wavelength of 1570 nm. (f) The simulated velocity of the liquid as a function of time under LCP (gray) and RCP (blue) at the point (0, 0, 200 nm). (g) Optofluidic CD spectrum, $CD_v(\lambda)$; (h) Spectrum of the optofluidic g-factor, $g_v(\lambda)$.

surface plasmon resonance under the CPL illumination. This temperature gradient can induce buoyance-driven natural convection of the surrounding fluid. Chiral fluid convection is clearly illustrated under CPL illumination, as shown in Figure 5. We only study the fluid convection of a single resonator because the photothermal contribution from neighboring NPs can be neglected in the sparse resonator distribution.[38] To better observe the convection effect, the incident flux was set to be $I_0 = 10^5$ W/cm^2 in our research on optofluidic property in this paper. The temperature distribution in the surrounding water is governed by eq 9. The temperature increase ΔT of the unit cell at t = 8 ns results in a laminar regime and Rayleigh–Benard-like fluid convection around the chiral resonator, as shown in Figure 5a–d. As illumination time increases, the velocity improves because of the increased temperature, as shown in Figure S7 (20 ns case). The fluid undergoes some reduction of mass density and thus produces an upward convection of the fluid (Archimedes force) because of the temperature increase that takes place within the fluid around the structure.[17] Because of fluidic continuity, the fluid in other places will flow toward the center of mass reduction in a toroidal shape. The profile of the fluid velocity is described by Navier–Stokes equation:[17]

$$\frac{\partial}{\partial t}\mathbf{v}(\boldsymbol{r}, t) + (\mathbf{v}(\boldsymbol{r}, t)\cdot\nabla)\mathbf{v}(\boldsymbol{r}, t) = \nu\nabla^2\mathbf{v}(\boldsymbol{r}, t) + \boldsymbol{f}_{th}(T(\boldsymbol{r}, t)) \quad (16)$$

$$\boldsymbol{f}_{th}(T) = \beta g \delta T(\boldsymbol{r}, t)\boldsymbol{u}_z \quad (17)$$

where ν is the viscosity of water and f_{th} the force per unit mass due to temperature nonuniformity. g is the gravitational acceleration, β is the dilatation coefficient of water, $\delta T(\boldsymbol{r}, t)$ is the temperature increase. $\boldsymbol{u}_z$ is the upward unit vector along the z-direction. Panels a and b of Figure 5 are taken from the LH structure under the illumination of LCP and RCP, respectively. These two patterns are similar in shape, but the value of temperature and velocity under LCP illumination is much higher than under RCP illumination. For the LH structure, the density of the streamlines located in the upper right corner of the chiral resonator is higher than that of the streamlines in the left corner, indicating a stronger fluidic motion was

https://doi.org/10.1021/acsnano.1c05658
ACS Nano XXXX, XXX, XXX–XXX

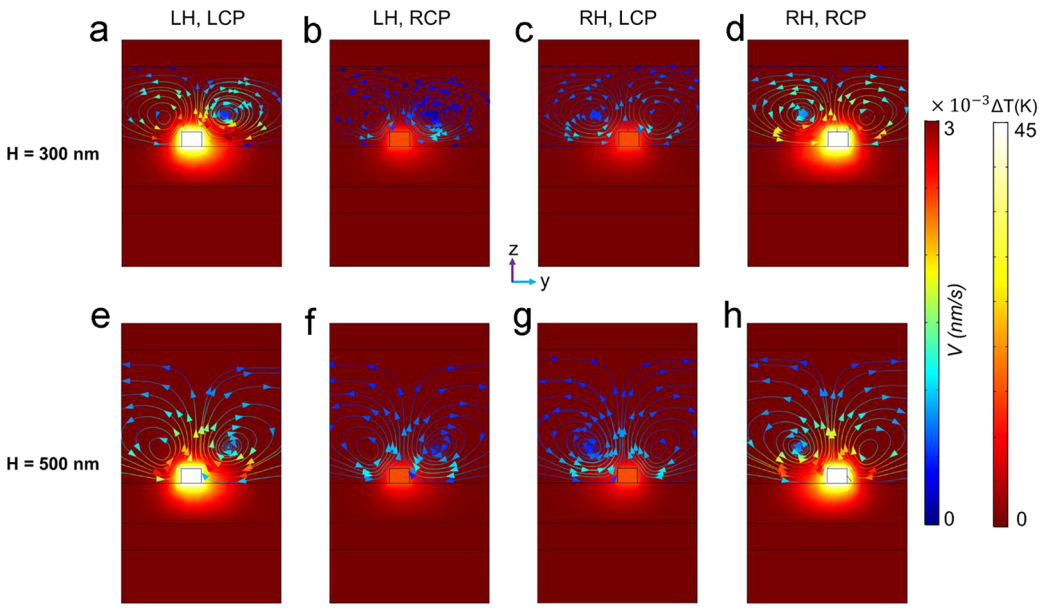

Figure 6. Influence of the chamber height *H* on thermal-induced convection. Temperature and velocity patterns (streamlines) with the height of the water is 300 nm (a–d) and 500 nm (e–h). Panels (a, e) and (b, f) are taken from the LH structure under the illumination of LCP and RCP, respectively. Panels (c, g) and (d, h) are taken from the RH structure under the illumination of LCP and RCP, respectively.

accumulated in the upper right corner of the resonator. The relatively large velocity of the surrounding fluid is mainly concentrated near the surface of the top structure and then gradually decreases as it moves away from the top resonator. The convection in the *xy* plane (t = 8 and 20 ns) is shown in Figures S8 and S9, respectively. They show asymmetric streamlines in the horizontal cross-section (z = 55 nm, 200 nm). The different patterns of the streamlines between the LH and RH structure stem from the chirality of the resonator, which provides us with ideas for controlling fluid motion. Similarly, the result mentioned above is also applicable to the RH structure, as shown in Figure 5c,d.

Figure 5e plots the evolution of the average temperature increase of the fluid as a function of time. As time increases, the temperature of the fluid (with RH enantiomer) gradually rises and reaches a steady temperature ∼35 K, and ∼10 K at t ≈ 2000 ns, with RCP and LCP excitation. Figure 5f plots the evolution of the chiral velocity of the thermal-induced fluid convection monitored at point (0, 0, 200 nm) as a function of time. It should be noted that for a single small nanostructure, plasmon-assisted fluid motion hardly exceeds 1 nm/s due to the extremely low Reynolds number.[4] We term circular dichroism velocity, CD_v, as shown in Figure 5g. The formula of CD_v is written as

$$CD_v(\lambda) = \mathbf{v}_{LCP}(\mathbf{r}, \lambda) - \mathbf{v}_{RCP}(\mathbf{r}, \lambda) \tag{18}$$

where $\mathbf{v}_{LCP}(\mathbf{r}, \lambda)$ and $\mathbf{v}_{RCP}(\mathbf{r}, \lambda)$ are the velocity of the fluid induced by LCP and RCP light, respectively. The CD_v has been recorded at t = 5000 ns, and the resonant wavelength is almost the same as the CD spectra. Correspondingly, a chiral g-factor for thermal-induced fluid convection, g_v, is defined as

$$g_v = \frac{\mathbf{V}_{LCP} - \mathbf{V}_{RCP}}{(\mathbf{V}_{LCP} + \mathbf{V}_{RCP})/2} \tag{19}$$

The peaks of g_v are at 1355 and 1570 nm with a value of ∼0.81 and ∼1.30, respectively, indicating a strong asymmetry of the thermal-induced convection. In contrast, the thermal-induced convection of an achiral system is illustrated in Figure S10. There is no differential absorption of CPL for an achiral structure, thus the distribution of the convection under the incidence of LCP is just the same as that under LCP incidence. Moreover, the absorption decreased due to the variation of the structure, which results in the reduction of magnitude of the temperature rise and the fluid velocity.

The performance of the proposed MPA under oblique incidence is also investigated, as shown in Figure S11. As mentioned earlier, there are two absorption peaks at normal incidence, with the first and second stem from the selective absorption of RCP and LCP, respectively. As the incident angle increases, the absorption of LCP slightly increases at the first resonant peak while the absorption of RCP gradually decreases, accompanied by a redshift of the peak position. However, the change of the second absorption peak is opposite. As a result, the CD value significantly degrades with the incident angle increase. It exhibits a potential chiral flip effect because of the varying phase difference between the two spin states, which conversely influence waves' constructive and instructive interferences.[39] The influence of thermal-induced convection under oblique incidence is also studied, as shown in Figure S11d,e. We take the result of an incident angle of 10 degrees as an example; chiral photothermal effects and thermal-induced convection remain when the incident angle is 10°.

Finally, we investigate the influence of the height H of the liquid chamber on the fluid convection, as shown in Figure 6. A top cover slide is conventionally used to confine the liquid in the z-direction. As the H increases, more fluid around the chiral structure is driven to move. However, the amount of heat generated is limited because of the extremely small size of the structure; consequently, the fluid remains almost stationary when the height exceeds 1 μm, as shown in Figure S12. With a larger design of the resonator size, several hundred nanometers per second flow velocity may be expected when H is above 100 μm as predicted by the literature.[4] If the incident flux is increased to 10^6 W/cm^2, a velocity (exceeds 3 nm/s) that is a

https://doi.org/10.1021/acsnano.1c05658
ACS Nano XXXX, XXX, XXX−XXX

magnitude larger than the current velocity can be obtained, as shown in Figure S13. We would like to mention that the velocity in this paper hardly exceeds 10 nm/s because of the low Reynolds number. We only demonstrate a proof-of-concept of combining chirality and optofluidics. The velocity can be increased by different schemes that are beyond the scope of the discussion. For example, HfN has demonstrated outstanding photothermal conversion efficiency among ZrN, TiN, and Au nanorod because of its low scattering cross-section, and thus, plasmon-assisted fluid motion can be increased.[40] An experimental study showed that plasmonic nanoantennas coupled with indium−tin-oxide (ITO) substrate could generate μm s^{-1} fluid convection.[16] Also, one can use micrometer-sized plasmonic antennas or assemblies of NPs to boost velocity.

CONCLUSION

In this work, we describe chiral optofluidics induced by the chiral photothermal effect in a plasmonic absorptive metasurface. We can understand this concept in terms of absorption CD, photothermal CD, optofluidic CD, and circular dichroism velocity. In our metasurface, the dissymmetry factor, g_A, was calculated as 1.78, approaching the limit of 2 ($0< g_A < 2$), much higher than that in chiral biomolecules ($g_A \sim 10^{-3}$) and colloidal plasmonic nanoparticle ($g_A \sim 10^{-2}$); it is also higher than the dissymmetry factors in other metastructures ($g_A \sim 1.5$). The giant absorption CD generates strong photothermal CD and finally leads to chiral optofluidics induced by thermal effects. We evidence an asymmetric laminar regime and a Rayleigh−Benard-like fluid convection. Overall, the photothermal effects in the metasurface and optofluidic effect have been extensively studied; however, few studies have explored the chirality and the thermal-induced convection of such systems. To this end, our idea provides insight into the physics of the plasmonic metasurface and the photothermal effect by showing that the hydrodynamic phenomena can be chiral. The theoretical idea developed in this work will help the growing range of disciplines that leverage plasmonics and control fluid flow on the micro- or nanoscale. The chiral optofluidics can be potentially used for integrated fluidic devices, biochemistry, clinical biology, and those optofluidic applications sensitive to circularly polarized light. For example, our idea can be used for a 3D lens; by changing the Dean flow rate using CPL, both the shape and focal length could be altered to achieve the flexibility that cannot be achieved otherwise in solid microlens.

MATERIALS AND METHODS

Simulation is performed in this paper by addressing photothermal and thermal-induced convection in the COMSOL Multiphysics software using finite element modeling. The electromagnetic properties of the structure are achieved by solving Maxwell's equation using the electromagnetic wave, frequency domain module. The optical absorption, electric/magnetic field distribution, charge distribution, and so forth, can be studied. The absorptance is defined as $A = 1 - R$, where R is the reflectance of the structure. We set up two orthogonally polarized planewaves with a phase difference of 90° to simulate the CPL. The light perpendicularly impinges onto the upper surface of the chiral MPA. The surrounding medium is chosen to be air or water. For spatial-temporal distribution calculation, the boundary conditions in the heat transfer equation (eq 9) are set as $T = T_0 = 293.15$ K for both the uppermost and nethermost boundaries. The chiral MPA is illuminated under pulsed excitation. The physical parameters for optical and thermal calculation are listed in Table S2. The fluid convection is modeled by using the heat transfer and laminar flow modules to solve eqs 9, 16, 17. Open boundaries are considered in fluid flow. The physical parameters for fluid convection calculation are listed in Table S3.

ASSOCIATED CONTENT

Supporting Information

The Supporting Information is available free of charge at https://pubs.acs.org/doi/10.1021/acsnano.1c05658.

The phase of the absorber around the resonant wavelength; the effect of three parameters (including period, the thickness of the dielectric layer, the thickness of chiral resonators) on CD, and the enhancement of magnetic field profile; the photothermal effect in air, the saturation effect of CD_T, and the photothermal conversion efficiency; the thermal-induced convection in different sections and irradiation time and the performance of the MPA under oblique incidence; the comparison of CD and g-factor between this paper and selected publications, the thermal and optical parameters of the materials, and the liquid parameters (PDF)

AUTHOR INFORMATION

Corresponding Authors

Peng Yu − *College of Optoelectronic Technology, Chengdu University of Information Technology, Chengdu 610225, China;* orcid.org/0000-0002-0242-7003; Email: ypeng@cuit.edu.cn

Alexander O. Govorov − *Department of Physics & Astronomy, Ohio University, Athens, Ohio 45701, United States;* orcid.org/0000-0003-1316-6758; Email: govorov@ohio.edu

Hongxing Xu − *School of Physics and Technology, Key Laboratory of Artificial Micro- and Nano-structures of Ministry of Education, Wuhan University, Wuhan 430072, China*; Email: hxxu@whu.edu.cn

Zhiming Wang − *Institute of Fundamental and Frontier Science, University of Electronic Science and Technology of China, Chengdu 610054, China; Yangtze Delta Region Institute (Huzhou), University of Electronic Science and Technology of China, Huzhou 313001, China*; Email: zhmwang@uestc.edu.cn

Authors

Cuiping Ma − *Institute of Fundamental and Frontier Science, University of Electronic Science and Technology of China, Chengdu 610054, China*

Wenhao Wang − *Institute of Fundamental and Frontier Science, University of Electronic Science and Technology of China, Chengdu 610054, China;* orcid.org/0000-0003-4171-1821

Yisong Zhu − *Institute of Fundamental and Frontier Science, University of Electronic Science and Technology of China, Chengdu 610054, China*

Feng Lin − *Institute of Fundamental and Frontier Science, University of Electronic Science and Technology of China, Chengdu 610054, China*

Jiaying Wang − *Institute of Fundamental and Frontier Science, University of Electronic Science and Technology of China, Chengdu 610054, China*

Zhimin Jing − *Institute of Fundamental and Frontier Science, University of Electronic Science and Technology of China, Chengdu 610054, China*

https://doi.org/10.1021/acsnano.1c05658
ACS Nano XXXX, XXX, XXX−XXX

Xiang-Tian Kong − *School of Physics, Nankai University, Tianjin 300071, China*
Peihang Li − *Institute of Fundamental and Frontier Science, University of Electronic Science and Technology of China, Chengdu 610054, China*
Dong Liu − *Department of Mechanical Engineering, University of Houston, Houston, Texas 77204-4006, United States*

Complete contact information is available at: https://pubs.acs.org/10.1021/acsnano.1c05658

Author Contributions

The manuscript was written through contributions of all authors. All authors have approved the final version of the manuscript.

Notes

The authors declare no competing financial interest.

ACKNOWLEDGMENTS

P.Y. is funded by China Postdoctoral Science Foundation (No. 2019M663467), Sichuan Science and Technology Program (No. 2020YJ0041), and the National Natural Science Foundation of China (No. 62005037). The authors acknowledge the support from the National Key Research and Development Program (No. 2019YFB2203400).

REFERENCES

(1) Baffou, G.; Quidant, R. Thermo-Plasmonics: Using Metallic Nanostructures as Nano-Sources of Heat. *Laser Photonics Rev.* **2013**, *7*, 171−187.
(2) Yue, S.; Lin, F.; Zhang, Q.; Epie, N.; Dong, S.; Shan, X.; Liu, D.; Chu, W.-K.; Wang, Z.; Bao, J. Gold-Implanted Plasmonic Quartz Plate as a Launch Pad for Laser-Driven Photoacoustic Microfluidic Pumps. *Proc. Natl. Acad. Sci. U. S. A.* **2019**, *116*, 6580.
(3) Wang, Y.; Zhang, Q.; Zhu, Z.; Lin, F.; Deng, J.; Ku, G.; Dong, S.; Song, S.; Alam, M. K.; Liu, D.; Wang, Z.; Bao, J. Laser Streaming: Turning a Laser Beam into a Flow of Liquid. *Sci. Adv.* **2017**, *3*, No. e1700555.
(4) Baffou, G.; Cichos, F.; Quidant, R. Applications and Challenges of Thermoplasmonics. *Nat. Mater.* **2020**, *19*, 946−958.
(5) Takano, K.; Jin, E.; Schreck, E.; Smyth, J.; Dovek, M. Automatic Design Optimization of Plasmon Antenna for Thermally Assisted Magnetic Recording. *IEEE Trans. Magn.* **2009**, *45*, 3604−3607.
(6) Zhu, H.; Yi, F.; Cubukcu, E. Plasmonic Metamaterial Absorber for Broadband Manipulation of Mechanical Resonances. *Nat. Photonics* **2016**, *10*, 709−714.
(7) Huang, X.; Jain, P. K.; El-Sayed, I. H.; El-Sayed, M. A. Plasmonic Photothermal Therapy (PPTT) Using Gold Nanoparticles. *Lasers Med. Sci.* **2008**, *23*, 217.
(8) Zhang, C.; Kong, T.; Fu, Z.; Zhang, Z.; Zheng, H. Hot Electron and Thermal Effects in Plasmonic Catalysis of Nanocrystal Transformation. *Nanoscale* **2020**, *12*, 8768−8774.
(9) Wang, W.; Besteiro, L. V.; Liu, T.; Wu, C.; Sun, J.; Yu, P.; Chang, L.; Wang, Z.; Govorov, A. O. Generation of Hot Electrons with Chiral Metamaterial Perfect Absorbers: Giant Optical Chirality for Polarization-Sensitive Photochemistry. *ACS Photonics* **2019**, *6*, 3241−3252.
(10) Besteiro, L. V.; Yu, P.; Wang, Z.; Holleitner, A. W.; Hartland, G. V.; Wiederrecht, G. P.; Govorov, A. O. The Fast and the Furious: Ultrafast Hot Electrons in Plasmonic Metastructures. Size and Structure Matter. *Nano Today* **2019**, *27*, 120−145.
(11) Wu, Y.; Qu, Z.; Osman, A.; Cao, W.; Khokhar, A. Z.; Soler Penades, J.; Muskens, O. L.; Mashanovich, G. Z.; Nedeljkovic, M. Mid-Infrared Nanometallic Antenna Assisted Silicon Waveguide Based Bolometers. *ACS Photonics* **2019**, *6*, 3253−3260.
(12) Yu, P.; Besteiro, L. V.; Huang, Y.; Wu, J.; Fu, L.; Tan, H. H.; Jagadish, C.; Wiederrecht, G. P.; Govorov, A. O.; Wang, Z. Broadband Metamaterial Absorbers. *Adv. Opt. Mater.* **2019**, *7*, 1800995.
(13) Kong, X.-T.; Khosravi Khorashad, L.; Wang, Z.; Govorov, A. O. Photothermal Circular Dichroism Induced by Plasmon Resonances in Chiral Metamaterial Absorbers and Bolometers. *Nano Lett.* **2018**, *18*, 2001−2008.
(14) Adhikari, S.; Spaeth, P.; Kar, A.; Baaske, M. D.; Khatua, S.; Orrit, M. Photothermal Microscopy: Imaging the Optical Absorption of Single Nanoparticles and Single Molecules. *ACS Nano* **2020**, *14*, 16414−16445.
(15) Rafiei Miandashti, A.; Khosravi Khorashad, L.; Kordesch, M. E.; Govorov, A. O.; Richardson, H. H. Experimental and Theoretical Observation of Photothermal Chirality in Gold Nanoparticle Helicoids. *ACS Nano* **2020**, *14*, 4188−4195.
(16) Roxworthy, B. J.; Bhuiya, A. M.; Vanka, S. P.; Toussaint, K. C. Understanding and Controlling Plasmon-Induced Convection. *Nat. Commun.* **2014**, *5*, 3173.
(17) Donner, J. S.; Baffou, G.; McCloskey, D.; Quidant, R. Plasmon-Assisted Optofluidics. *ACS Nano* **2011**, *5*, 5457−5462.
(18) Zhu, J.; Zhu, X.; Zuo, Y.; Hu, X.-j.; Shi, Y.; Liang, L.; Yang, Y. Optofluidics: The Interaction between Light and Flowing Liquids in Integrated Devices. *Opto-Electron. Adv.* **2019**, *2*, 19000701.
(19) Jin, C. M.; Lee, W.; Kim, D.; Kang, T.; Choi, I. Photothermal Convection Lithography for Rapid and Direct Assembly of Colloidal Plasmonic Nanoparticles on Generic Substrates. *Small* **2018**, *14*, 1803055.
(20) Ren, Y.; Qi, H.; Chen, Q.; Li, Y.; Ruan, L. Optofluidic Control Using Light Illuminated Plasmonic Nanostructure as Microvalve. *Int. J. Heat Mass Transfer* **2019**, *133*, 1019−1025.
(21) Jones, S.; Andrén, D.; Antosiewicz, T. J.; Stilgoe, A.; Rubinsztein-Dunlop, H.; Käll, M. Strong Transient Flows Generated by Thermoplasmonic Bubble Nucleation. *ACS Nano* **2020**, *14*, 17468−17475.
(22) Baral, S.; Green, A. J.; Livshits, M. Y.; Govorov, A. O.; Richardson, H. H. Comparison of Vapor Formation of Water at the Solid/Water Interface to Colloidal Solutions Using Optically Excited Gold Nanostructures. *ACS Nano* **2014**, *8*, 1439−1448.
(23) Rodrigo, J. A.; Angulo, M.; Alieva, T. Tailored Optical Propulsion Forces for Controlled Transport of Resonant Gold Nanoparticles and Associated Thermal Convective Fluid Flows. *Light: Sci. Appl.* **2020**, *9*, 181.
(24) Zhu, X.; Cicek, A.; Li, Y.; Yanik, A. A. Plasmofluidic Microlenses for Label-Free Optical Sorting of Exosomes. *Sci. Rep.* **2019**, *9*, 8593.
(25) Hentschel, M.; Schäferling, M.; Duan, X.; Giessen, H.; Liu, N. Chiral Plasmonics. *Sci. Adv.* **2017**, *3*, No. e1602735.
(26) Khorashad, L. K.; Besteiro, L. V.; Correa-Duarte, M. A.; Burger, S.; Wang, Z. M.; Govorov, A. O. Hot Electrons Generated in Chiral Plasmonic Nanocrystals as a Mechanism for Surface Photochemistry and Chiral Growth. *J. Am. Chem. Soc.* **2020**, *142*, 4193−4205.
(27) Liu, T.; Besteiro, L. V.; Liedl, T.; Correa-Duarte, M. A.; Wang, Z.; Govorov, A. O. Chiral Plasmonic Nanocrystals for Generation of Hot Electrons: Toward Polarization-Sensitive Photochemistry. *Nano Lett.* **2019**, *19*, 1395−1407.
(28) Wang, B.; Yu, P.; Wang, W.; Zhang, X.; Kuo, H.-C.; Xu, H.; Wang, Z. M. High-Q Plasmonic Resonances: Fundamentals and Applications. *Adv. Opt. Mater.* **2021**, *9*, 2001520.
(29) Wang, J.; Chen, Y.; Chen, X.; Hao, J.; Yan, M.; Qiu, M. Photothermal Reshaping of Gold Nanoparticles in a Plasmonic Absorber. *Opt. Express* **2011**, *19*, 14726−14734.
(30) Li, W.; Coppens, Z. J.; Besteiro, L. V.; Wang, W.; Govorov, A. O.; Valentine, J. Circularly Polarized Light Detection with Hot Electrons in Chiral Plasmonic Metamaterials. *Nat. Commun.* **2015**, *6* (1), 8379.
(31) Zhu, Y.; Xu, H.; Yu, P.; Wang, Z. Engineering Plasmonic Hot Carrier Dynamics toward Efficient Photodetection. *Appl. Phys. Rev.* **2021**, *8* (2), No. 021305.

(32) Fasman, G. D. *Circular dichroism and the conformational analysis of biomolecules*; Springer Science & Business Media: New York, 2013; pp 7−19.
(33) Ma, W.; Kuang, H.; Xu, L.; Ding, L.; Xu, C.; Wang, L.; Kotov, N. A. Attomolar DNA Detection with Chiral Nanorod Assemblies. *Nat. Commun.* **2013**, *4*, 2689.
(34) Hentschel, M.; Schäferling, M.; Weiss, T.; Liu, N.; Giessen, H. Three-Dimensional Chiral Plasmonic Oligomers. *Nano Lett.* **2012**, *12*, 2542−2547.
(35) Miao, X.; Wilson, B. K.; Lin, L. Y. Localized Surface Plasmon Assisted Microfluidic Mixing. *Appl. Phys. Lett.* **2008**, *92*, 124108.
(36) Jin, H.; Lin, G.; Bai, L.; Amjad, M.; Bandarra Filho, E. P.; Wen, D. Photothermal Conversion Efficiency of Nanofluids: An Experimental and Numerical Study. *Sol. Energy* **2016**, *139*, 278−289.
(37) Gao, R.; Fu, R.; Jiao, W.; Fan, G.; Liang, C.; Chen, J.; Ren, H.; Wang, Y.; Liu, W.; Ren, S.; Dong, Q.; Wei, Q.; Ren, X.; Sun, M.; Liu, W. Photothermal Effect of Au Nanoparticles and Photothermal Inactivation to Saccharomycetes cell. *Optik* **2020**, *206*, 163757.
(38) Baffou, G.; Berto, P.; Bermúdez Ureña, E.; Quidant, R.; Monneret, S.; Polleux, J.; Rigneault, H. Photoinduced Heating of Nanoparticle Arrays. *ACS Nano* **2013**, *7*, 6478−6488.
(39) Jing, L.; Wang, Z.; Yang, Y.; Zheng, B.; Liu, Y.; Chen, H. Chiral Metamirrors for Broadband Spin-Selective Absorption. *Appl. Phys. Lett.* **2017**, *110*, 231103.
(40) Karaballi, R. A.; Esfahani Monfared, Y.; Dasog, M. Photothermal Transduction Efficiencies of Plasmonic Group 4 Metal Nitride Nanocrystals. *Langmuir* **2020**, *36*, 5058−5064.

https://doi.org/10.1021/acsnano.1c05658
ACS Nano XXXX, XXX, XXX−XXX